THESIS FOR THE DEGREE OF LICENTIATE OF
PHILOSOPHY

Nanostructured electromagnetic metasurfaces at optical frequencies

Nils ODEBO LÄNK

Department of Physics
Chalmers University of Technology
Göteborg, Sweden, 2016

ii

NANOSTRUCTURED ELECTROMAGNETIC METASURFACES AT OPTICAL FRE-
QUENCIES
Nils Odebo Länk

Cover:
*(Left) Scanning electron microscope (SEM) images of metasurfaces of polycrys-
talline silicon nanopillars. (Right) Sketch of the radiation pattern of a single dipole
above an air-glass interface.*

CHALMERS UNIVERSITY OF TECHNOLOGY

Nanostructured electromagnetic metasurfaces at optical frequencies
Nils ODEBO LÄNK

Department of Physics

Licentiate of Philosophy

Abstract

Electromagnetic metasurfaces are broadly defined as optically thin layers that are structured on the subwavelength scale. In general, metasurfaces thus consist of nanoparticles, or other kinds of "meta-atom", arranged in some pattern where both the individual particle sizes and the inter-particle distances are much smaller than the wavelength. With advances in nanofabrication, it has become feasible to precisely engineer metasurface constituent elements to fulfil certain functions.

This thesis, focuses on the properties of metasurfaces assembled by colloidal lithography. In contrast to most metasurfaces studied in the literature, samples produced by colloidal lithography lack long-range periodicity. Two different approaches to metasurface design are investigated. In appended papers I and II, the individual elements are plasmonic gold nanoparticles while appended paper III deals with the geometric resonances supported in silicon nanoparticles. The investigated systems are able to convert propagating electromagnetic fields into localized ones and vice-versa. Hence, we can measure information about local properties in the far-field.

In paper I, the individual particles were progressively tilted with respect to the substrate normal, resulting in an overall directional response. This directionality was manifested in enhanced fluorescence emission in particular directions.

In paper II, the ability of anisotropic individual particles to alter the polarization of the incoming light beam was utilized to develop a sensing scheme based on the detection of rotation of polarization. The change in rotation and ellipticity of the light was shown to be sensitive to the local refractive index around the particles. Refractometric biosensing was performed by tracking these changes in real time.

The interaction between the incident light and geometric electric and magnetic resonances was studied in paper III. At certain illumination conditions, it was shown that the interference between interface reflection and the coherent scattering from the electric and magnetic dipole resonances gave rise to almost complete light absorption independent of polarization.

The ability to design metasurfaces with specific properties is of importance for future applications. The results presented in this thesis contribute to the understanding of the properties of the individual particles that compose a metasurface and how structuring of these particles affects its overall properties.

Keywords: metasurfaces, plasmonics, geometric resonances, high-index nanophotonics, colloidal lithography, nanostructures

List of publications

The following papers are included in this thesis:

I **Directional Light Extinction and Emission in a Metasurface of Tilted Plasmonic Nanopillars**
Ruggero Verre, Mikael Svedendahl, Nils Odebo Länk, Zhong-Jian Yang, Gülis Zengin, Tomasz Antosiewicz and Mikael Käll.
Nano Letters, 2016, 16, 98 – 104.

II **Polarization conversion-based molecular sensing using anisotropic plasmonic metasurfaces**
Ruggero Verre, Nicolo Maccaferri, Karsten Fleischer, Mikael Svedendahl, Nils Odebo Länk, Alexandre, Dmitriev, Paolo Vavassori, Igor Shvets, and Mikael Käll.
Nanoscale, 2016, 8, 10576 – 10581.

III **Large-scale silicon nanophotonic metasurfaces with polarization independent near perfect absorption**
Nils Odebo Länk, Ruggero Verre and Mikael Käll.
In manuscript

My contributions:

I I performed analytical modelling of scattering based on numerical simulations.

II I designed and performed numerical simulations for scattering, absorption and near-fields, participated in the development of an analytical model as well as drafting parts of the paper.

III I performed the optical experiments, designed and performed the numerical simulations and drafted the paper.

Acknowledgements

I would like acknowledge the support of my supervisor Professor Mikael Käll, for the guidance, the opportunity and for always keeping your door open. You have been patient and very knowledgeable.

Thank you to my co-supervisor Professor Peter Johansson, for the great theoretical understanding. Your extensive knowledge and your way of seeing things has influenced me. Thank you for always taking the time to answer my questions.

Dr. Ruggero Verre, for the enormous support in our projects. Without your help, I would have been lost and probably stuck with optical alignment or not having a clue what to write. You have always been positive and energetic. Your motivation has been infectious and very helpful.

Dr. Tomasz Antosiewicz, for our very pleasant conversations about the ins and outs of Lumerical and other simulation methods. Your help and support has greatly expedited my learning.

Dr. Mikael Svedendahl, for the many discussions at the very beginning of my stay. Your help made the initial process much easier.

Thank you also to Peter Apell, for being there, even though I rarely used the opportunity.

Dr. Robin Ogier, both for discussions and for the nice times spend outside work, at bars or with card games.

My thanks go also to the rest of the Bionanophotonics group, past and new! Specifically, Zhong-Jian, Lei, Srdjan, Timur and Yurui for all the help with various issues, Daniel for the conversations, both personal and professional and Martin for putting up with me when sharing rooms at various events.

Thank you also to my family and friends, who have always supported me and cheered for me throughout my studies. It has been a great help to know that I always have you.

Contents

Chapter 1

Introduction to metasurfaces

The interaction between light and matter is one of the most important and ubiquitous concepts in our everyday lives. Light interacts with objects around us and the photoreceptors in our eyes. This interaction shapes how we perceive the world through sight.

Recent advances in nanotechnology have allowed for the fabrication of tailored structures at the nanoscale. The control of light by means of nanostructured surfaces has resulted in many new real-life applications. Examples of such applications include biological sensors, gas detectors and solar cells [1–3]. The objective is to design new materials able to either manipulate the light wavefront in certain ways or to use properties of the single constituent elements to realize remarkable functionalities.

In effect, visible light interacting with nanoparticles is completely analogous to micro- and radio waves interacting with antennas. The function of an antenna is to convert propagating waves into localized electric signals or vice versa. In some contexts, nanoparticles are therefore referred to as "optical antennas". They are able to convert visible light into enhanced near-fields as well as transmit information about local properties into the far-field. Researchers attempting to design optical antennas can benefit greatly from decades of research in radio frequency antenna engineering.

It is a common practice to combine several radio antenna elements into an antenna array. This gives great control of the shape of the radiation pattern. Deliberate assembly of nanoparticles into different patterns has become the focus of considerable recent research. Through various nanofabrication techniques, it is possible to assemble many nanoparticles smaller than the wavelength of visible light into a pattern such that the inter-particle distances are also subwavelength. The resulting "antenna assembly" is referred to as a metasurface. A characteristic property of metasurfaces is that they are able to abruptly change the properties of the incident light field over a subwavelength distance scale. Controllable changes of the polarization, amplitude or phase of light can be obtained through careful design [4].

Metallic nanoparticles with plasmonic resonances in the visible or infrared spectral range can act as optical antennas and offer opportunities to engineer light-matter interactions at the nanoscale. Examples range from light bending, focusing and polarization control [5–7] to optical holography [8]. Other than directly altering the properties of light, plasmonic metasurfaces offer great opportunities in sensing of refractive index changes or using Surface-enhanced Raman Spectroscopy [2, 9–12].

In addition to plasmonic metasurfaces, extensive attention has been dedicated to metasurfaces composed of nanostructures fabricated from high index dielectric materials such as silicon or germanium. These nanoparticles possess tunable electric and magnetic geometric dipole resonances in the visible and near infrared spectral range. The resonant behaviour in high index nanoparticles has been harnessed for applications in phase manipulation, sensing, surface-enhanced spectroscopies and subwavelength imaging [13–16].

Most metasurfaces studied in the literature are periodic arrangements of subwavelength antennas. Such metasurfaces are generally easier to describe and lend themselves to electromagnetic simulation using periodic boundary conditions. In this thesis, we focus on metasurfaces fabricated with colloidal lithography [17]. As a consequence of the fabrication procedure, samples produced using this technique lack long-range periodicity while still having a well defined nearest neighbour distance. It is the aim of this thesis to elucidate the optical properties of such metasurfaces by analyzing the individual nanoantenna and the collective behaviour. Metasurfaces composed of metallic and high-index nanoparticles are considered.

Chapter 2 deals with metallic nanoparticles and their plasmonic properties. A general background of the optical properties of metals is followed by a description of the behaviour of plasmonic nanoparticles. Finally, it is explained how the optical properties of plasmonic nanoparticles can be used for sensing based on refractive index change.

In Chapter 3, the resonant properties of high index dielectric nanoparticles are explained using the exact Mie solution for spheres. This is followed by a description of the optical properties of silicon nanoparticles, specifically nanopillars on top of a glass substrate.

After having probed general optical properties of the different individual metamaterial constituent elements considered, attention is turned in Chapter 4 to methods used for explaining the optical properties of metasurfaces.

Finally, Chapter 5 provides a summary of the presented work along with an outlook for future my metasurface research.

Chapter 2

Plasmonics

The field of plasmonics has been a very active area of research for the last twenty years. A plasmonic excitation is an oscillation of the free conduction electrons in a metal. One distinguishes between a surface plasmon polariton (SPP) and a localized surface plasmon resonance (LSPR). An SPP is a charge oscillation that propagates along the interface between a metal and a dielectric, while an LSPR oscillation lives at the surface of a nanoparticle.

LSPR oscillations couple extremely well to light and their interaction cross sections can greatly exceed their geometrical cross sections. The spectral position (colour) of these resonances is greatly dependent on the geometric shape and size of the nanoparticles as well as the properties of their immediate surroundings. Colloidal solutions of metal nanoparticles with the right sizes typically have vibrant and beautiful colours, something which was utilized in making stained glass windows for medieval churches.

The first appearances of a mathematical description of plasmonic waves date back to the end of the 19th century and early 20th century. For SPPs, with Sommerfeld's work on radio waves [18] and for LSPRs, with Mie's description of resonances in small particles [19]. It took the work of Ugo Fano [20] to connect this theoretical work to observed effects in the visible wavelength range.

The interaction of light with plasmonic nanostructures has been extensively researched in the last decades. Applications of such structures include the sensing based on refractive index changes [1, 9, 21] discussed in Section 2.3, Surface-enhanced Raman Scattering (SERS) even down to single molecule detection [12, 22] as well as improved solar cells, a review of which can be found in Ref. [3].

2.1   Drude model

The linear optical properties of any material are described by the frequency dependent dielectric function, $\varepsilon(\omega)$ (since the magnetic response $\mu(\omega)$, is negligible at optical frequencies). For dielectric materials, this is often (confusingly) referred to as the dielectric constant since it is real, positive and tends to be only weakly frequency dependent in the visible spectral region. The optical properties of metals have a more complicated dependence on frequency. Specifically, metals reflect incident light of microwave and radio frequencies but absorb light at near-infrared and visible frequencies. One of the simplest approximations of the complex dielectric function of metals is the Drude model (due to Paul Drude [23]). In this model, the conduction

electrons are modelled as a free electron gas under the influence of a driving electric field. The one-dimensional equation of motion takes the form of a driven, damped harmonic oscillator. We have

$$m_e \ddot{x}(t) + m_e \gamma \dot{x}(t) = -eE(x,t) \ , \tag{2.1}$$

where m_e, γ, e and E are the electron mass, the damping frequency (characteristic collision frequency), electron charge and the driving electric field, respectively. If we assume that the wavelength of the driving field is much larger than the relevant length scales of electron oscillation, we can disregard its position dependence. This approximation is valid for light of lower energy than extreme UV or soft x-rays. Furthermore, assuming a harmonic time dependence of the field and position, we can perform a Fourier transform and write

$$-\omega^2 x(\omega) - \mathrm{i}\omega\gamma x(\omega) = -\frac{e}{m_e} E_0(\omega) \ , \tag{2.2}$$

where ω is the angular frequency of the driving field and obtain

$$x(\omega) = \frac{e/m_e}{\omega^2 + \mathrm{i}\gamma\omega} E_0(\omega) \ . \tag{2.3}$$

With the concentration of electrons n, and the dipole moment per electron $p_e(\omega) = -ex(\omega)$, we can thus define a macroscopic polarization, or dipole moment per unit volume as

$$P(\omega) = -\frac{ne^2/m_e}{\omega^2 + \mathrm{i}\gamma\omega} E_0(\omega) \ . \tag{2.4}$$

With the assumption of a homogeneous and isotropic material, the polarization is $P(\omega) = \varepsilon_0(\varepsilon(\omega) - 1)E_0(\omega)$, and we can identify the Drude dielectric function as

$$\varepsilon(\omega) = 1 - \frac{ne^2/m_e\varepsilon_0}{\omega^2 + \mathrm{i}\gamma\omega} = 1 - \frac{\omega_p^2}{\omega^2 + \mathrm{i}\gamma\omega} \ , \tag{2.5}$$

where we have introduced the plasma frequency $\omega_p = \sqrt{ne^2/m_e\varepsilon_0}$. This simple model captures the most important effects of metallic optical properties. However, since the Drude model only considers the free conduction electrons it fails to take into account, for example, optical transitions from the valence band to the conduction band. These transitions contribute significantly to absorption and are especially important in the visible frequency region for noble metals such as gold.

2.2   Absorption and scattering

If we send an incident field toward an arbitrary particle and place a detector at infinity on the other side, some of the incident light will be lost. The total light lost is called *extinction*. From conservation of energy, we know that the scattered field from the particle must cancel the incident field at the detector with precisely an amount equal to the total extinction. Following

this line of reasoning leads to the demonstration of the optical theorem, which provides a very general expression for the extinction cross section [24]

$$\sigma_{\text{ext}} = \frac{1}{k_m|E_0|^2} \text{Im}\left\{ \left(\boldsymbol{E}_0^* \cdot \boldsymbol{e} \right)_{\theta=0} \right\} \ , \tag{2.6}$$

where $k_m = \sqrt{\varepsilon_m}\omega/c_0$ is the wave number of the medium, $\boldsymbol{e}$ is the scattering amplitude, and the incident field has a general polarization, $\boldsymbol{E}^{\text{inc}} = \boldsymbol{E}_0 \mathrm{e}^{\mathrm{i}k_m z}$. The scattering amplitude $\boldsymbol{e}$ is defined through the scattered far-field as

$$\boldsymbol{E}^{\text{scat}} = \frac{\mathrm{e}^{\mathrm{i}k_m r}}{4\pi r} \boldsymbol{e} \ . \tag{2.7}$$

The extinction cross section has the unit of area and is interpreted as an effective size of the particle in its interaction with light. For plasmonic nanoparticles, the extinction cross section can greatly exceed the geometric cross section implying that they interact extremely strongly with light.

The light lost in extinction is a sum of the light that is absorbed within the particle and the scattering in all directions other than the forward direction. The total scattering can be found through integrating the scattered far field on a large sphere surrounding the particle [24]

$$\sigma_{\text{sca}} = \frac{1}{(4\pi)^2|E_0|^2} \int_\Omega |e|^2 \, \mathrm{d}\Omega \ . \tag{2.8}$$

The total amount of light lost in extinction must be the sum of light lost in scattering and in absorption. Thus, the absorption cross section can be found as

$$\sigma_{\text{abs}} = \sigma_{\text{ext}} - \sigma_{\text{sca}} \ . \tag{2.9}$$

The definitions above are valid for any type of particle of any size. In order to elucidate the optical behaviour of metallic nanoparticles it is instructive to employ the electrostatics approximation. We assume, in the rest of the chapter, that our particle of interest is much smaller than the wavelength of the optical field. This allows us to disregard the position dependence of the field.

2.2.1 Particles smaller than the wavelength

Polarizability of a small sphere

We consider a sphere of radius a, with $a \ll \lambda$ and dielectric function $\varepsilon(\omega)$ in a homogeneous medium with relative dielectric constant ε_m. The sphere is subjected to a static electric field $\boldsymbol{E}_0 = E_0\hat{\boldsymbol{z}}$. Since our region of interest contains no charge distribution, we can solve the Laplace equation for the potential. Doing so results in the following expressions [24, 25] for the potential inside and outside the sphere (in spherical coordinates centered in

the sphere)

$$\Phi_{\text{inside}} = -\frac{3\varepsilon_m}{\varepsilon + 2\varepsilon_m} E_0 r \cos\theta \ , \tag{2.10}$$

$$\Phi_{\text{outside}} = -E_0 r \cos\theta + \frac{\varepsilon - \varepsilon_m}{\varepsilon + 2\varepsilon_m} E_0 a^3 \frac{\cos\theta}{r} \ . \tag{2.11}$$

Let us now turn our attention to the potential outside the sphere. The first term is the potential corresponding to the static field and the second term is actually the potential from an electric dipole with dipole moment

$$\boldsymbol{p}(\omega) = 4\pi\varepsilon_0\varepsilon_m a^3 \frac{\varepsilon(\omega) - \varepsilon_m}{\varepsilon(\omega) + 2\varepsilon_m} \boldsymbol{E}_0(\omega) \ . \tag{2.12}$$

The external field is said to *induce* a dipole in the sphere. We thus define the sphere's static polarizability, α^{s},

$$\alpha^{\text{s}} = 4\pi\varepsilon_0\varepsilon_m a^3 \frac{\varepsilon - \varepsilon_m}{\varepsilon + 2\varepsilon_m} \ , \tag{2.13}$$

such that $\boldsymbol{p} = \alpha^{\text{s}}\boldsymbol{E}_0$. Here we have dropped the (ω) functional dependence on the dielectric function of the sphere for brevity. Note that the polarizability defined here has units of $[\varepsilon_0]\text{m}^3$, or Asm^2/V while some authors choose to not include the $\varepsilon_0\varepsilon_m$ in the polarizability, simply giving it the units of volume.

Let us now consider a small sphere in vacuum, such that $\varepsilon_m = 1$. In this case, the real part of the denominator vanishes when $\text{Re}\{\varepsilon + 2\} = 0$, or $\text{Re}\,\varepsilon = -2$. The frequency where the condition is fulfilled and $\text{Im}\,\varepsilon \approx 0$ is sometimes referred to as the Fröhlich frequency. At this frequency, the sphere has a resonant polarizability, often referred to as a Localized Surface Plasmon Resonance (LSPR). In order to fulfil the condition, it is required that the sphere has a permittivity with a negative real part, something that is typically encountered in metals (for frequencies below the plasma frequency, ω_p). For this reason, LSPRs are typically associated with metal nanoparticles. For noble metals, such as gold and silver, the Fröhlich condition is fulfilled for visible frequencies.

In the next sections, we extend the sphere polarizability in Eq. (2.13) to more general circumstances.

Radiation reaction

When the external field is not quite static but has a finite frequency, the polarizability in Eq. (2.13) is not quite exact [26]. To realize this, consider a single non-absorbing (ε real) sphere in a non-absorbing medium illuminated by a plane wave. The sphere will scatter the radiation and the far field in the forward direction will have been attenuated. The sphere is therefore required to have a dipole moment which has components out of phase with the incident plane wave. In other words, the polarizability must be complex (but Eq. (2.13) with a real ε is not).

To deal with the dipole scattering, we introduce a "radiative reaction"

term analogous to the treatment in [25]. The idea is to add a radiative reaction field to the expression for the total field

$$\boldsymbol{E}_{\text{tot}}(\boldsymbol{r}_0) = \boldsymbol{E}_0(\boldsymbol{r}_0) + \boldsymbol{E}_{\text{rad}}(\boldsymbol{r}_0) \ . \tag{2.14}$$

The trick is to require that the work done by $\boldsymbol{E}_{\text{rad}}$ is balanced by the energy radiated by a dipole.

The total rate of work done by the radiative reaction field inside the volume V is given by following integral [25]

$$\left\langle \frac{\mathrm{d}W^{\text{rad}}}{\mathrm{d}t} \right\rangle = \frac{1}{2}\text{Re} \int_V \mathrm{d}^3r \, \boldsymbol{j}^*(\boldsymbol{r}) \cdot \boldsymbol{E}_{\text{rad}}(\boldsymbol{r}) \ , \tag{2.15}$$

where $\boldsymbol{j}(\boldsymbol{r})$ is the current distribution. For a point dipole, $\boldsymbol{p}$, at $\boldsymbol{r} = \boldsymbol{r}_0$, it is given by $\boldsymbol{j}(\boldsymbol{r}) = -\mathrm{i}\omega\boldsymbol{p}\delta^{(3)}(\boldsymbol{r} - \boldsymbol{r}_0)$ and the total power radiated by a dipole is [25]

$$P^{\text{rad}}(\omega) = \frac{k_m^3}{12\pi}\frac{\omega}{\varepsilon_0\varepsilon_m}|\boldsymbol{p}|^2 \ . \tag{2.16}$$

Balancing Eqns. (2.15) and (2.16), we can identify

$$\boldsymbol{E}_{\text{rad}}(\boldsymbol{r}_0) = \frac{\mathrm{i}k_m^3}{6\pi\varepsilon_0\varepsilon_m}\boldsymbol{p} \ . \tag{2.17}$$

For external fields with $\lambda \gg a$, we can still make the approximation that the field remains static across the particle volume and use the polarizability in (2.13). Using the total field for the dipole moment yields

$$\boldsymbol{p} = \alpha^{\text{s}}\boldsymbol{E}_{\text{tot}} = \alpha^{\text{s}}\left(\boldsymbol{E}_0(\boldsymbol{r}_0) + \frac{\mathrm{i}k_m^3}{6\pi\varepsilon_0\varepsilon_m}\boldsymbol{p} \right) \ . \tag{2.18}$$

Solving for $\boldsymbol{p}$ allows us to define a modified polarizability α such that $\boldsymbol{p} = \alpha\boldsymbol{E}_0$ that takes this radiation reaction into account

$$\alpha = \frac{\alpha^{\text{s}}}{1 - \mathrm{i}k_m^3\alpha^{\text{s}}/(6\pi\varepsilon_0\varepsilon_m)} \ . \tag{2.19}$$

Depolarization

Another effect that is usually corrected for in the case of an external field with a finite frequency is the finite size of the scatterer. We still assume that the wavelength of the external field is much larger than the radius of the sphere. However, there is a correction to the total field at the center of the sphere due to the presence of polarized matter around it, we have

$$\boldsymbol{E}_{\text{tot}}(\boldsymbol{r}_0) = \boldsymbol{E}_0(\boldsymbol{r}_0) + \boldsymbol{E}_{\text{dep}}(\boldsymbol{r}_0) \ . \tag{2.20}$$

One can derive a form for this depolarization field up to order k_m^3 [27] by assuming a homogeneous polarization of the sphere and calculating the

contribution to the field at the center of the sphere from each volume element, then

$$\boldsymbol{E}_{\text{dep}}(\boldsymbol{r}_0) = \frac{\mathrm{i}k_m^3}{6\pi\varepsilon_0\varepsilon_m}\boldsymbol{p} + \frac{k_m^2}{4\pi\varepsilon_0\varepsilon_m}\boldsymbol{p} \ . \tag{2.21}$$

Defining a modified polarizability by solving for $\boldsymbol{p}$ yields

$$\alpha = \frac{\alpha^{\mathrm{s}}}{1 - \mathrm{i}k_m^3\alpha^{\mathrm{s}}/(6\pi\varepsilon_0\varepsilon_m) - k_m^2\alpha^{\mathrm{s}}/(4\pi\varepsilon_0\varepsilon_m a)} \ . \tag{2.22}$$

Note that this modified polarizability also includes the radiation reaction term obtained in the previous section. This is because taking into account the retarded dipole fields from each volume element also accounts for their radiation loss.

This correction is usually called the MLWA (Modified Long-Wavelength Approximation). The effects of the MLWA modifications are secondary for small particles but start playing a crucial role for particles of sizes of the order of $a \sim 30$ nm and illumination with visible light. In particular, the resonances broaden and shift towards lower energies.

Anisotropic particles

So far, we have only considered the optical response of spherical shapes. It turns out that it is difficult to analytically obtain the form of the potential in all but very few cases. In the case of ellipsoidal symmetry, however, it is possible to obtain polarizabilities. In this case, when the spherical symmetry is broken, the polarizability becomes a tensor. For an ellipsoid with semi-axes $a_1 \geq a_2 \geq a_3$ in a *static* field (compare to the spherical polarizability in Eq. (2.13)), the diagonal polarizability tensor is [24]

$$\alpha_{ii}^{\mathrm{s}} = \frac{4\pi\varepsilon_0\varepsilon_m a_1 a_2 a_3}{3}\frac{\varepsilon - \varepsilon_m}{\varepsilon_m + L_i(\varepsilon - \varepsilon_m)} \ , \tag{2.23}$$

where $i = 1, 2, 3$ and L_i is called the geometric factor. It is given by

$$L_i = \frac{a_1 a_2 a_3}{2}\int_0^\infty \frac{\mathrm{d}q}{(a_i^2 + q)\sqrt{(a_1^2 + q)(a_2^2 + q)(a_3^2 + q)}} \ , \tag{2.24}$$

and they obey the constraint

$$L_1 + L_2 + L_3 = 1 \ . \tag{2.25}$$

For a sphere, $a_1 = a_2 = a_3$ and we have $L_1 = L_2 = L_3 = \frac{1}{3}$. The integral above is well-behaved and rapidly converging. Analytical, closed-form expressions exist, however, for the special cases of prolate ($a_1 > a_2 = a_3$, "cigar-shaped") and oblate ($a_1 = a_2 > a_3$, "pancake-shaped") spheroids [24].

In an analogous way to that of spheres, one usually defines a modified polarizability for ellipsoids in the MLWA [28] as

$$\alpha_{ii} = \frac{\alpha_{ii}^{\mathrm{s}}}{1 - \mathrm{i}k_m^3\alpha_{ii}^{\mathrm{s}}/(6\pi\varepsilon_0\varepsilon_m) - k_m^2\alpha_{ii}^{\mathrm{s}}/(4\pi\varepsilon_0\varepsilon_m a_i)} \ . \tag{2.26}$$

This modified polarizability was used in appended papers I and II to model the effects of anisotropy.

The effects of this anisotropy is a splitting of the resonance modes. For a sphere, a single, 3-fold degenerate resonance is present due to symmetry. When the spherical symmetry is broken, this degeneracy is lifted and distinct resonances appear in the new eigendirections. In particular, for constant volume, the resonance in the elongated direction shifts toward lower energies due to a reduction in the restoring force, and vice versa for the compressed direction.

Optical cross sections

In previous sections, we presented different ways of obtaining the dipole moment for subwavelength structures through their polarizability (tensor).

The optical cross sections in Eqns. (2.6) and (2.8) can then be evaluated using the scattering amplitude from a dipole source. The far field scattering amplitude from a dipole, $\boldsymbol{p}$ is given by [25]

$$\boldsymbol{e} = \frac{k_m^2}{\varepsilon_0 \varepsilon_m} (\hat{\boldsymbol{r}} \times \boldsymbol{p}) \times \hat{\boldsymbol{r}} \ . \tag{2.27}$$

Using the appropriate dipole polarizability to express the dipole moment as $\boldsymbol{p} = \overset{\leftrightarrow}{\alpha} \cdot \boldsymbol{E}_0$, we obtain

$$\sigma_{\text{ext}} = \frac{k_m}{|E_0|^2} \text{Im} \left\{ \boldsymbol{E}_0^* \cdot \frac{\overset{\leftrightarrow}{\alpha}}{\varepsilon_0 \varepsilon_m} \cdot \boldsymbol{E}_0 \right\} \ , \tag{2.28}$$

where we used the fact that $\boldsymbol{E}_0$ and $\hat{\boldsymbol{r}}$ are perpendicular in the forward direction. For the scattering cross section, eq. (2.8) results in

$$\sigma_{\text{sca}} = \frac{k_m^4}{(4\pi\varepsilon_0\varepsilon_m)^2 |E_0|^2} \int_\Omega \left| \boldsymbol{p} - (\hat{\boldsymbol{r}} \cdot \boldsymbol{p})\hat{\boldsymbol{r}} \right|^2 \mathrm{d}\Omega \ . \tag{2.29}$$

Since the integral is over the entire solid angle, it must be independent on the dipole's orientation and we can without loss of generality choose this to be in the z-direction. Using $\hat{\boldsymbol{r}} \cdot \hat{\boldsymbol{z}} = \cos\theta$, we obtain

$$\sigma_{\text{sca}} = \frac{k_m^4}{6\pi |E_0|^2} \left| \frac{\overset{\leftrightarrow}{\alpha}}{\varepsilon_0 \varepsilon_m} \cdot \boldsymbol{E}_0 \right|^2 \ . \tag{2.30}$$

Recall from eq. (2.9) that the absorption cross section can be found through the extinction and scattering as

$$\sigma_{\text{abs}} = \sigma_{\text{ext}} - \sigma_{\text{sca}} \ . \tag{2.31}$$

2.3 Plasmonics-assisted refractometric sensing

The optical response of a plasmonic nanoparticle is greatly dependent on its immediate dielectric environment. This can be qualitatively understood by once again looking at the polarizability for a small sphere, Eq. (2.13),

repeated here

$$\alpha^{\mathrm{s}}(\omega) = 4\pi\varepsilon_0\varepsilon_m a^3 \frac{\varepsilon(\omega) - \varepsilon_m}{\varepsilon(\omega) + 2\varepsilon_m} \; , \tag{2.13}$$

where $\varepsilon(\omega), \varepsilon_m$ are the dielectric functions of the sphere and its surrounding medium, respectively. As discussed in Sec. 2.2.1, the resonance occurs where the real part of the denominator vanishes, $\mathrm{Re}\{\varepsilon(\omega) + 2\varepsilon_m\} = 0$. Using the Drude model for the permittivity of a metal sphere, Eq. (2.5), we get

$$\omega_{\mathrm{res}} = \sqrt{\frac{\omega_p^2}{1 + 2\varepsilon_m} - \gamma^2} \; . \tag{2.32}$$

We can clearly see that a change in the refractive index, $n_m = \sqrt{\varepsilon_m}$, of the surrounding medium changes the frequency of the resonance. In particular, an increase in the refractive index causes a redshift of the resonance.

The SPP, the propagating counterpart to the LSPR discussed above is analogously sensitive to its local dielectric environment. This property was first used as a biosensor in the beginning of the 1980s [29, 30]. The method has since evolved enormously and sensing devices are commercially available. SPP-based sensing was reviewed in Ref. [31].

For localized surface plasmon resonances (LSPRs), the first experimental demonstration of biosensing came in 1998 [1]. A review of LSPR-based biosensing can be found in Ref. [21].

A direct comparison between the two methods for refractometric sensing was performed in Ref. [32] showing similar performance.

For anisotropic nanostructures, there exist distinct plasmon resonances in the different principal directions (see e.g. the ellipsoidal polarizability in Eq. (2.23)). As a result, incident light polarized along a direction that excites both these resonances will accumulate a polarization rotation and ellipticity. A local refractive index change affects the different plasmon resonances differently and a change in rotation and ellipticity can be measured. In appended paper II, this effect was used to demonstrate a bulk refractive index sensing scheme as well as real-time molecular sensing.

Chapter 3

High-index nanophotonics

The early research on metasurfaces was mainly related to localized plasmon resonances as discussed in Chapter 2. The light cannot be confined for long periods of time in these resonances, however, due to large Ohmic loss. This loss also leads to local heating of the nanoparticles which can be useful for certain applications such as drug release [33] or tumour treatment [34]. The local heating can in many cases be detrimental, however. In recent years, a lot of research has been devoted to metasurfaces and metamaterials composed of nanoparticles made from high-refractive index materials such as silicon [35, 36]. These materials have very low absorptive loss and can thus be very useful in cases where high quality resonances are desired or local heating is unwanted.

Dielectric nanoparticles with high refractive index support electric and magnetic geometric resonances [36–38] within the visible and near-infrared wavelength range. The properties of high index nanoparticles have very recently been used for various applications including refractive index sensing [14], directionality [13, 39, 40] and subwavelength imaging [16].

In this chapter, we aim to shed some light on the optical properties of subwavelength particles composed of high-index dielectrics.

3.1 Mie resonances

The problem of the optical response of an arbitrary sphere can be solved analytically. The solution was presented by Gustav Mie in 1908 [19] and thus bears the name Mie theory. By solving the Maxwell equations exactly in spherical symmetry, expressions for the electric and magnetic fields in any point in space can be found. Thus, the scattering, absorption and extinction for a sphere of radius a can be calculated from converging infinite series of multipoles according to [24]

$$\sigma_{\text{ext}} = \frac{2\pi}{k_m^2} \sum_{n=1}^{\infty} (2n+1)\text{Re}\{a_n + b_n\} \,, \tag{3.1}$$

$$\sigma_{\text{sca}} = \frac{2\pi}{k_m^2} \sum_{n=1}^{\infty} (2n+1)\left(|a_n|^2 + |b_n|^2\right) \,, \tag{3.2}$$

where a_n, b_n are called scattering coefficients and are expressed in terms of spherical Bessel functions as

$$a_n = \frac{\mu_m m^2 j_n(mx) \big[x j_n(x)\big]' - \mu_s j_n(x) \big[mx j_n(mx)\big]'}{\mu_m m^2 j_n(mx) \big[x h_n^{(1)}(x)\big]' - \mu_s h_n^{(1)}(x) \big[mx j_n(mx)\big]'} \ , \qquad (3.3)$$

$$b_n = \frac{\mu_s j_n(mx) \big[x j_n(x)\big]' - \mu_m j_n(x) \big[mx j_n(mx)\big]'}{\mu_s j_n(mx) \big[x h_n^{(1)}(x)\big]' - \mu_m h_n^{(1)}(x) \big[mx j_n(mx)\big]'} \ , \qquad (3.4)$$

where $x = k_m a$ is the size parameter, $m = k_m/k_s$ is the relative refractive index, k_m, μ_m, k_s, μ_s are the wavenumbers and permeabilities for the surrounding medium and the sphere, respectively.

Although these expressions are exact if not truncated, they are not transparent and the physics in them is obscured. We note that the first scattering coefficients, a_1 and b_1, correspond to electric and magnetic dipoles, respectively. The corresponding dipole polarizabilities for plane wave incidence can be found by normalizing by the correct partial-wave amplitude of the incident wave [36, 41] , we have

$$\alpha_e = \mathrm{i} \frac{6\pi \varepsilon_0 \varepsilon_m}{k_m^3} a_1 \ , \qquad (3.5)$$

$$\alpha_m = \mathrm{i} \frac{6\pi}{k_m^3} b_1 \ . \qquad (3.6)$$

The above polarizabilities exactly describe the electric and magnetic dipole response for an arbitrary sphere. For the plasmonic nanoparticles discussed in Chapter 2, the electric dipole response is often sufficient. In particular, one can note that Eq. (3.5) reduces to the polarizability of a sphere in a static field, Eq. (2.13) in the limit $k_m \to 0$. Typically, one uses this approximation (with the corrections discussed in Sec. 2.2.1) while still taking into account the frequency dependence of the dielectric function. This allows one to capture most of the physics and avoid drowning in Bessel functions.

3.2   Silicon nanostructures

For spheres made of high refractive index materials such as silicon ($n \approx 4$ in the visible) the electric and magnetic Mie dipole resonances show up in the visible. Figure 3.1 shows the scattering efficiency (scattering cross section normalized by geometric area) calculated using Eq. (3.2). The red and blue curves show the contributions from the electric and magnetic dipole scattering, a_1 and b_1, respectively. The dashed purple curve shows the sum of electric and magnetic contributions while the black curve shows the full Mie sum, truncated at convergence. It is clear that a description using only electric and magnetic dipole scattering is sufficient in this regime.

In paper III, we studied metasurfaces composed of silicon nanopillars on top of a glass substrate. These were fabricated from polycrystalline silicon wafers using colloidal lithography. The dielectric function for the polycrystalline silicon was measured using ellipsometry. Figure 3.2 shows the measured dielectric function and corresponding refractive index along with data taken from Ref. [42] for monocrystalline silicon.
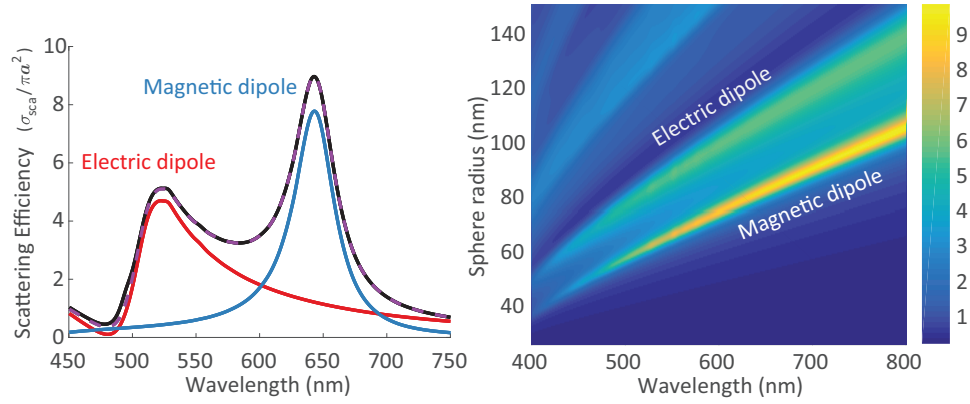
FIGURE 3.1: (Left) The scattering efficiency for a crystalline silicon sphere of radius $a = 80$ nm in vacuum, calculated using Mie theory. (Right) The scattering efficiency of silicon spheres of different radius calculated using Mie theory using only the electric and magnetic dipole terms, a_1 and b_1. The dielectric function for silicon was taken from Ref. [42].
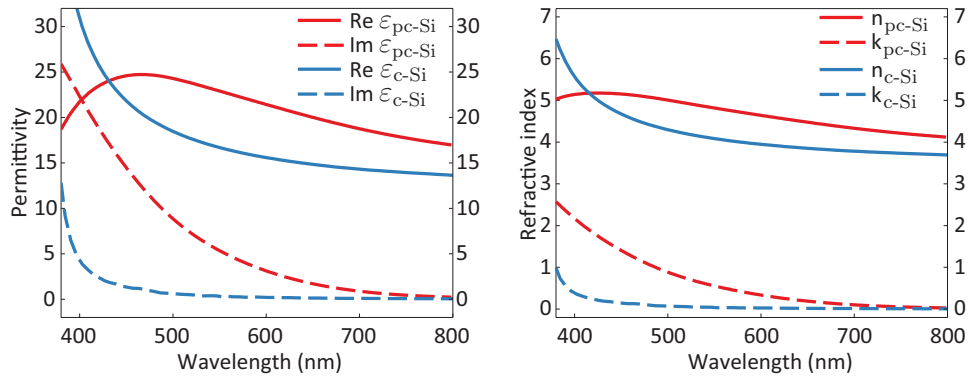

FIGURE 3.2: (Left) The dielectric function and (Right) refractive index of different types of silicon. The red curves show the data measured by ellipsometry for the polycrystalline silicon wafers used to fabricate metasurfaces. The blue curves show data taken from Ref. [42] for crystalline silicon.
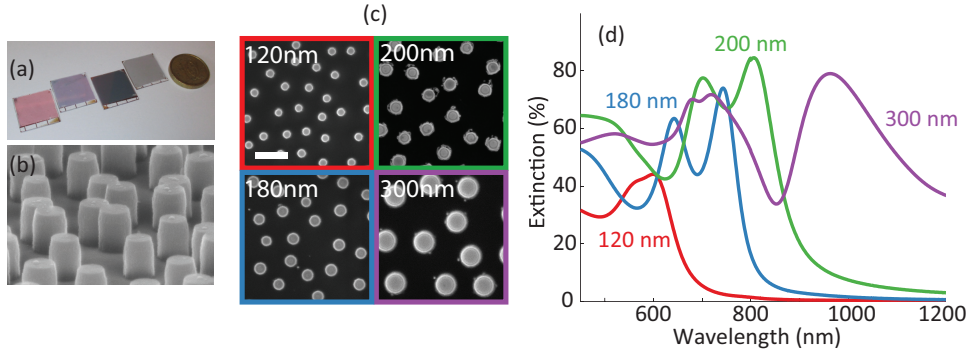
FIGURE 3.3: (a) Photograph of the fabricated metasurfaces.
(b) Tilted view SEM-image of typical metasurface. (c) SEM
images of the measured metasurfaces. The scale bar corre-
sponds to 500 nm. (d) Measured extinction for the samples
with silicon nanopillars of different diameters. The electric
and magnetic dipole resonances are clearly visible.

The imaginary part of the dielectric function governs absorption in the material. For monocrystalline silicon, the imaginary part is essentially zero above $\lambda = 500$ nm and it is widely regarded as a dielectric material in this regime. The band-gap of silicon at room temperature is $E_g = 1.124$ eV [43], so for higher wavelengths than $\lambda \approx 1100$ nm the silicon electrons do not absorb any light (for higher wavelengths there can be absorption by phonons).

The higher absorption in the polycrystalline silicon is mainly due to losses at grain boundaries but may also be due to impurities.

The fabricated samples were characterized using scanning electron microscopy (SEM) and optical spectroscopy (as discussed in Sec. 4.5), see Fig. 3.3. The extinction spectra in Fig. 3.3(d) show resonances in the visible and near infrared spectral range that are of the same character as the geometric Mie resonances in spheres shown in Fig. 3.1.

The separation into electric and magnetic dipole polarizabilities is usually done for dielectric particles of any shape in this size regime ($D \sim 80 - 200$ nm). Here, the optical response is dominated by the Mie modes of electric and magnetic dipole character in the visible and near infrared.

The electric and magnetic dipole moments of any structure can be calculated from the following [25]

$$\boldsymbol{p} = \int_V \boldsymbol{P}(\boldsymbol{r})\, \mathrm{d}^3 r = \int_V \varepsilon_0 \big(\varepsilon(\boldsymbol{r}) - 1\big) \boldsymbol{E}(\boldsymbol{r})\, \mathrm{d}^3 r\ , \tag{3.7}$$

$$\boldsymbol{m} = \frac{1}{2} \int_V \boldsymbol{r} \times \boldsymbol{J}(\boldsymbol{r})\, \mathrm{d}^3 r = \frac{-\mathrm{i}\omega}{2} \int_V \varepsilon_0 \big(\varepsilon(\boldsymbol{r}) - 1\big) \boldsymbol{r} \times \boldsymbol{E}(\boldsymbol{r})\, \mathrm{d}^3 r\ , \tag{3.8}$$

where $\boldsymbol{P}(\boldsymbol{r})$ is the polarization, $\boldsymbol{J}(\boldsymbol{r})$ is the current density. We have assumed no free sources, so $\boldsymbol{J}(\boldsymbol{r}) = -\mathrm{i}\omega \boldsymbol{P}(\boldsymbol{r})$ is the displacement current density. The electric and magnetic polarizabilities can then be identified through $\boldsymbol{p} = \vec{\boldsymbol{\alpha}}^{\,\mathrm{e}} \cdot \boldsymbol{E}_{\mathrm{exc}}$ and $\boldsymbol{m} = \vec{\boldsymbol{\alpha}}^{\,\mathrm{m}} \cdot \boldsymbol{H}_{\mathrm{exc}}$ where $\boldsymbol{E}_{\mathrm{exc}}$, $\boldsymbol{H}_{\mathrm{exc}}$ are the exciting fields (the fields that would exist at the centre of the particle in its absence).

Figure 3.4 shows the scattering efficiency for a crystalline silicon sphere of radius $a = 80$ nm. The solid lines are calculated from Mie theory, Eq. (3.2) using only the lowest order scattering coefficients, a_1 (red solid line)
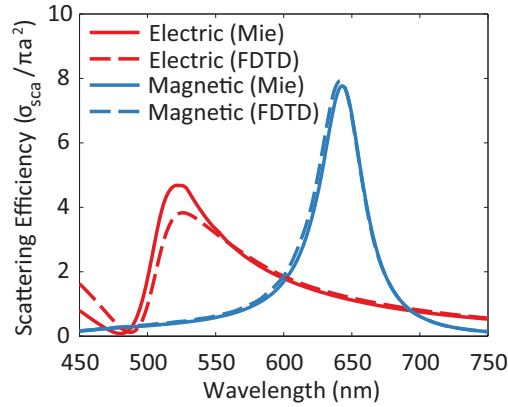
FIGURE 3.4: The scattering efficiency for a crystalline silicon sphere of radius $a = 80$ nm in vacuum, calculated using Mie theory (solid lines) and from polarizabilities extracted from FDTD (dashed lines). The dielectric function for silicon used in both cases was taken from Ref. [42].

and b_1 (blue solid line). The dashed lines show the scattering efficiency calculated from polarizabilities extracted through Eqns. (3.7) and (3.8). The electric fields in this case were extracted from a full electromagnetic wave simulation using the Finite Difference Time-Domain (FDTD) method (see Sec. 4.4).

The modal decomposition using Eqns. (3.7) and (3.8) with fields from FDTD was used in appended paper III to describe the response of the individual silicon nanopillars on top of a glass substrate. The presence of the substrate induces coupling effects between the different modes [44] and some mixing can be observed (see also appended paper III).

Fig. 3.5 shows the scattering efficiency at normal incidence for polycrystalline nanopillars of different radii and diameters on top of a glass substrate calculated using FDTD with the dielectric function measured using ellipsometry (see red curves in Fig. 3.2). The resonance positions for the electric and magnetic dipole modes are clearly less sensitive to the height of the nanopillar than to its radius. In addition, the electric and magnetic resonances scale differently. This allows for the possibility of placing the electric and magnetic resonances at specific wavelengths through precise engineering of the nanoparticle dimensions.
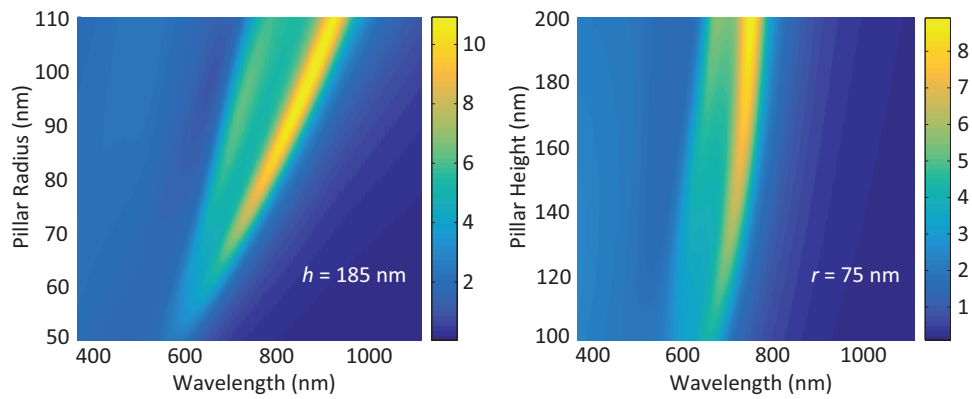
FIGURE 3.5: Scattering efficiencies for polycrystalline sili-
con nanopillars on top of a glass substrate calculated from
FDTD at normal incidence. The dielectric function used in
the simulations was measured using ellipsometry for bulk
wafers. (Left) The scattering efficiency as a function of di-
ameter for pillars of fixed height, $h = 185$ nm. Note that the
resonance wavelengths for both electric and magnetic scale
approximately linearly with radius. (Right) The scattering
efficiency as a function of height for pillars of fixed radius
$r = 75$ nm.

Chapter 4

Methods

The work presented in this thesis is mainly focused on analytical considerations and numerical simulations. However, some optical spectroscopy measurements have been performed.

The main methods used have been a Green's function approach to the radiation of a dipole in the presence of an interface, an analytical effective medium theory and computational full wave electromagnetic simulations using the Finite Difference Time-Domain (FDTD) method. The effective medium, or island-film, theory was used to model the optical response of metasurfaces and FDTD was used to characterize the optical response of single nanoparticles. A background and description of these methods will be the focus of this chapter. In addition, a brief description of the Coupled Dipole Approximation (CDA), although not employed in the appended papers, is included for completeness.

4.1 Dipole fields in the presence of an interface

The metasurface samples studied in this work are mainly fabricated with the Hole-Mask Colloidal Lithography technique [17]. Such samples are typically composed of nanoparticles patterned on top of a glass slide. Since these nanoparticles are in most cases smaller than the wavelength of visibile light, the approximations made in Section 2.2.1 are generally applicable and the particles are treated as dipoles. Consequently, it is important to understand how electric dipoles scatter when in presence of a dielectric interface.

We follow a similar procedure to [45] and start by noting that the electric field at a point $\boldsymbol{r}$ from a current distribution $\boldsymbol{j}$ is given by

$$\boldsymbol{E}(\boldsymbol{r}) = \mathrm{i}\omega\mu_0\mu_j \int \mathrm{d}^3 r'\overset{\leftrightarrow}{\boldsymbol{G}}(\boldsymbol{r},\boldsymbol{r}')\cdot\boldsymbol{j}(\boldsymbol{r}')\,, \tag{4.1}$$

where $\overset{\leftrightarrow}{\boldsymbol{G}}(\boldsymbol{r},\boldsymbol{r}')$ is the Green's function tensor of the surrounding environment and μ_j is the relative permeability of the medium. For a point dipole in with strength $\boldsymbol{p}_0$ at $\boldsymbol{r} = \boldsymbol{r}_0$, we have $\boldsymbol{j} = -\mathrm{i}\omega\boldsymbol{p}_0\delta^{(3)}(\boldsymbol{r}-\boldsymbol{r}_0)$ and the field becomes

$$\boldsymbol{E}(\boldsymbol{r}) = \omega^2\mu_0\mu_j\overset{\leftrightarrow}{\boldsymbol{G}}(\boldsymbol{r},\boldsymbol{r}_0)\cdot\boldsymbol{p}_0\,. \tag{4.2}$$

To get an expression for the dipole scattering, we thus need to identify the Green's function tensor of the environment.

We introduce a single interface at $z = 0$, dividing regions of space with permittivities and permeabilities ε_j, μ_j. Let $j = 1$ for $z > 0$ and $j = 2$ for
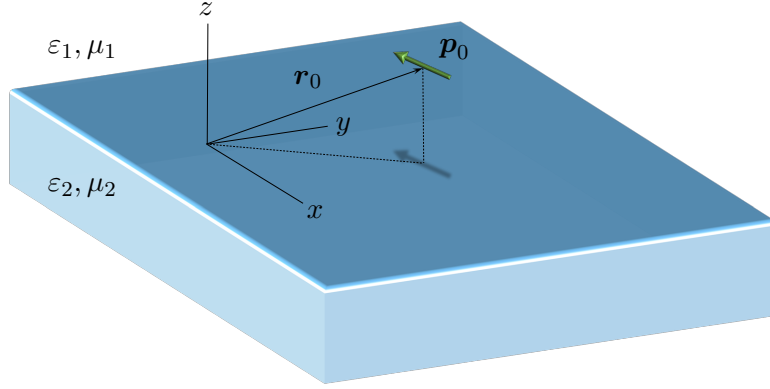
FIGURE 4.1: Spatial configuration of the dipole above a planar interface. The dipole with strength $\boldsymbol{p}_0$ is located at $\boldsymbol{r}_0$

$z < 0$. We also assume that the sources are located in medium 1, so that $z_0 > 0$. The parallel momentum, $q_\parallel$, is conserved along the interface as a consequence of the boundary conditions (Snell's law) and we denote the z-component of the wave number in medium j by p_j. With these notations, we have $k_j = \sqrt{\varepsilon_j}\omega/c_0$ and $k_j^2 = q_\parallel^2 + p_j^2$.

In the case of a layered structure, or specifically a single interface, the background is translationally invariant in the parallel directions x and y, or $\boldsymbol{r}_\parallel$. This means that the Green's function is also translationally invariant in these directions and has a spatial dependence of the form $\overleftrightarrow{\boldsymbol{G}}(\boldsymbol{r}, \boldsymbol{r}') = \overleftrightarrow{\boldsymbol{G}}(\boldsymbol{r}_\parallel - \boldsymbol{r}'_\parallel, z, z')$. It can thus be Fourier transformed in the parallel directions. This allows us to express the electric field in Eq. (4.2) in terms of the Fourier transform of the Green's Function (GFFT), we have

$$\boldsymbol{E}(\boldsymbol{r}) = \omega^2 \mu_0 \mu_j \int \frac{\mathrm{d}^2 q_\parallel}{(2\pi)^2} \overleftrightarrow{\boldsymbol{G}}(\boldsymbol{q}_\parallel, z, z_0) \cdot \boldsymbol{p}_0 \, \mathrm{e}^{\mathrm{i}\boldsymbol{q}_\parallel \cdot \boldsymbol{R}_\parallel} \, , \qquad (4.3)$$

where we introduced $\boldsymbol{R}_\parallel = \boldsymbol{r}_\parallel - \boldsymbol{r}_{0,\parallel}$. The point of introducing the Fourier transform is to write the field in terms of a superposition of plane waves, in Eq. (4.3). This is because it is well known how plane waves interact with an interface, through Fresnel reflection and refraction, so we can treat each of these plane waves separately.

We introduce a direction of propagation for the field and define its wave vector, $\vec{q}_j^{\,\tau}$, as follows

$$\boldsymbol{q}_j^{\pm} = \boldsymbol{q}_\parallel \pm p_j \hat{\boldsymbol{z}} = (q_x, q_y, \pm p_j) \, , \qquad (4.4)$$

where $\tau = +$ denotes upward propagation ($z > z_0$) and $\tau = -$ denotes downward propagation ($z < z_0$). The corresponding unit vector to $\vec{q}_j^{\,\tau}$ is $\hat{\boldsymbol{q}}_j^{\,\tau} = \vec{q}_j^{\,\tau}/k_j$. The z-component of the wave number can be expressed as $p_j = k_j \cos\theta_j$, where θ_j is the angle of incidence or refraction, measured from the substrate normal, $\hat{\boldsymbol{z}}$. Note that θ_j becomes complex in the case of evanescent waves (as in the case of total internal reflection). At this point, it is also convenient to introduce the unit vectors for s- and p-polarization, $\hat{\boldsymbol{s}}_j^{\,\tau}$ and $\hat{\boldsymbol{p}}_j^{\,\tau}$. These vectors are defined with respect to planes normal to z. We

have

$$\hat{\boldsymbol{s}}_j^\pm = \frac{\hat{\boldsymbol{z}} \times \hat{\boldsymbol{q}}_j^\pm}{|\hat{\boldsymbol{z}} \times \hat{\boldsymbol{q}}_j^\pm|} = \frac{1}{q_\parallel}(-q_y,\, q_x,\, 0)\ , \tag{4.5}$$

and

$$\hat{\boldsymbol{p}}_j^\pm = \hat{\boldsymbol{s}}_j^\pm \times \hat{\boldsymbol{q}}_j^\pm = \frac{1}{k_j}\left(\pm\frac{q_x}{q_\parallel}p_j,\, \pm\frac{q_y}{q_\parallel}p_j,\, -q_\parallel\right)\ . \tag{4.6}$$

Since the unit vector for s-polarization is independent of direction of propagation, we will henceforth drop its τ-superscript. The triad $\{\hat{\boldsymbol{q}}_j^\tau,\, \hat{\boldsymbol{p}}_j^\tau,\, \hat{\boldsymbol{s}}_j\}$ forms a basis for $\mathbb{R}^3$, meaning

$$\hat{\boldsymbol{q}}_j^\tau \otimes \hat{\boldsymbol{q}}_j^\tau + \hat{\boldsymbol{p}}_j^\tau \otimes \hat{\boldsymbol{p}}_j^\tau + \hat{\boldsymbol{s}}_j \otimes \hat{\boldsymbol{s}}_j = \mathbb{1}\ , \tag{4.7}$$

where $\otimes$ denotes the dyadic (or outer) product. For column vectors, $\boldsymbol{v} \otimes \boldsymbol{v} = \boldsymbol{v}\boldsymbol{v}^T$. With these definitions, it can be shown that (see e.g. [46]) the GFFT for a *homogeneous* medium (that is, not our layered environment) is

$$\overleftrightarrow{\boldsymbol{G}}_{\mathrm{h}}^\tau(\boldsymbol{q}_\parallel, z, z_0) = \frac{\mathrm{i}}{2p_j}\left(\hat{\boldsymbol{p}}_j^\tau \otimes \hat{\boldsymbol{p}}_j^\tau + \hat{\boldsymbol{s}}_j \otimes \hat{\boldsymbol{s}}_j\right)\mathrm{e}^{\mathrm{i}p_j|z-z_0|}\ . \tag{4.8}$$

The dipole will emit a field composed of a superposition of plane waves. These plane waves will then reflect from and transmit through the interface. Treating each plane wave of each polarization separately, we can identify the fields above and below the interface. Above, it will be a sum of a direct field and a reflected field and below it will simply be a transmitted field. We have

$$\boldsymbol{E}_j(\boldsymbol{r}) = \begin{pmatrix} E^p \\ E^s \end{pmatrix} = \frac{\mathrm{i}\omega^2\mu_0\mu_j}{2}\int\frac{\mathrm{d}^2q_\parallel}{(2\pi)^2}\begin{pmatrix} \boldsymbol{M}_j^p(\boldsymbol{q}_\parallel)\cdot\boldsymbol{p}_0 \\ \boldsymbol{M}_j^s(\boldsymbol{q}_\parallel)\cdot\boldsymbol{p}_0 \end{pmatrix}\mathrm{e}^{\mathrm{i}\boldsymbol{q}_\parallel\cdot\boldsymbol{R}_\parallel}\mathrm{e}^{\mathrm{i}p_j|z|}\ , \tag{4.9}$$

where the vectors $\boldsymbol{M}_j^{p/s}(\boldsymbol{q}_\parallel)$ contain the information about the interaction with the interface. They are, explicitly

$$\boldsymbol{M}_1^p(\boldsymbol{q}_\parallel) = \frac{1}{p_1}\left(\hat{\boldsymbol{p}}_1^+\mathrm{e}^{-\mathrm{i}p_1z_0} + r^p(\boldsymbol{q}_\parallel)\hat{\boldsymbol{p}}_1^-\mathrm{e}^{\mathrm{i}p_1z_0}\right)\ , \tag{4.10}$$

$$\boldsymbol{M}_1^s(\boldsymbol{q}_\parallel) = \frac{1}{p_1}\left(\mathrm{e}^{-\mathrm{i}p_1z_0} + r^s(\boldsymbol{q}_\parallel)\mathrm{e}^{\mathrm{i}p_1z_0}\right)\hat{\boldsymbol{s}}_1\ , \tag{4.11}$$

$$\boldsymbol{M}_2^p(\boldsymbol{q}_\parallel) = \frac{1}{p_2}\frac{p_2}{p_1}t^p(\boldsymbol{q}_\parallel)\mathrm{e}^{\mathrm{i}p_1z_0}\hat{\boldsymbol{p}}_1^-\ , \tag{4.12}$$

and

$$\boldsymbol{M}_2^s(\boldsymbol{q}_\parallel) = \frac{1}{p_2}\frac{p_2}{p_1}t^s(\boldsymbol{q}_\parallel)\mathrm{e}^{\mathrm{i}p_1z_0}\hat{\boldsymbol{s}}_1\ . \tag{4.13}$$

Here, $r^{s/p}$ and $t^{s/p}$ are the regular Fresnel coefficients for reflection and transmission. Note that these depend on the parallel momentum (in other words, the angle). This method can easily be generalized to a situation with

multiple layers of dielectrics beneath the dipole source. One then needs to extract the reflection and transmission coefficients for all layers, through a transfer matrix method (see e.g. [47]). One also needs to add a phase compensation to the fields in the lowest medium to account for the total thickness of the layered structure [45].

Far fields

In the previous section, we derived the form of the electric field from a dipole above an interface. What is interesting for an experiment though, is the radiation pattern – the field that propagates to the far field.

For large r, we can obtain the asymptotic form of the integral in Eq. (4.3) using the method of stationary phase, or saddle point method (see eg. [48]). We get

$$\boldsymbol{E}_{j,\text{far}}(\boldsymbol{r}) = \begin{pmatrix} E_{\text{far}}^p \\ E_{\text{far}}^s \end{pmatrix} = \frac{\omega^2 \mu_0 \mu_j}{4\pi} \frac{\mathrm{e}^{\mathrm{i}k_j r}}{r} p_j \begin{pmatrix} \boldsymbol{M}_j^p(q_\parallel^0) \cdot \boldsymbol{p}_0 \\ \boldsymbol{M}_j^s(q_\parallel^0) \cdot \boldsymbol{p}_0 \end{pmatrix} , \qquad (4.14)$$

where $q_\parallel^0$ is the parallel momentum corresponding to the direction of observation, i.e. $\boldsymbol{r}$. Special care needs to be taken when looking at the transmitted fields, since in that case the θ-angle refers to the "angle of refraction" in the Fresnel coefficient.

These expressions were employed in appended paper I to model the directional scattering of tilted plasmonic gold nanopillars on top of a glass substrate.

We turn for a moment to the specific case of the metasurface samples where the top medium is air ($n_1 = 1$) and the lower medium is glass ($n_2 = 1.52$). One interesting thing to note about this type of dipole radiation is that some number of the plane waves in the superposition in Eq. (4.3) are evanescent in air. Having a higher refractive index, the glass can support a larger range of parallel momenta, however, and some of those aforementioned plane waves can become propagating in the glass. This radiation is called "forbidden", since it propagates above the critical angle, θ_c. Since the evanescent waves decay exponentially in air, the forbidden radiation is highly dependent on the distance of the dipole to the interface, z_0, see Fig. 4.2.

The reverse of this effect, by reciprocity, is used in total internal reflection microscopy to enhance spatial contrast [49]. When illuminating an interface at an angle above the critical angle, all transmitted waves are evanescent. However, if there is a for example a fluorophore close enough to the interface, it can be excited by the evanescent waves and fluoresce into the air side. Due to the strong dependence on z_0, only fluorophores very close to the surface will give a signal.

4.2   Island-film theory

From the Maxwell equations it follows that the electric and magnetic fields at either side of the boundary between two different media have certain boundary conditions. Applying vector calculus theorems allows one to identify these boundary conditions [25]. The standard Fresnel coefficients
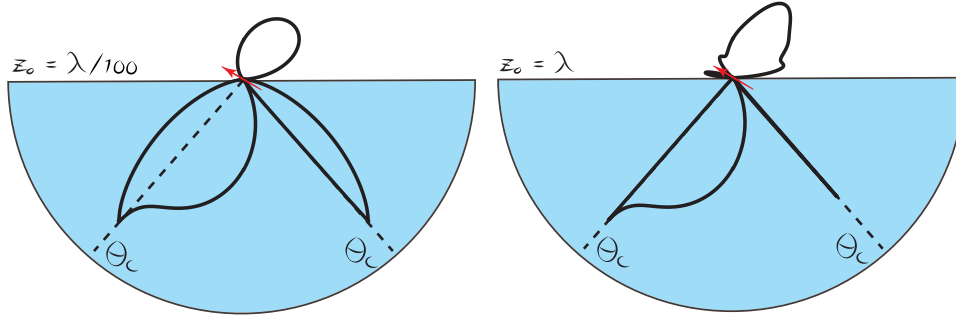
FIGURE 4.2: Far field radiation patterns of a 30° tilted dipole in air above a planar glass ($n_2 = 1.52$) interface. The two images show the dipole at different distances from the interface. Notice that the radiation into the "allowed" zone is independent of z_0 while the radiation into the "forbidden" zone is not.

for reflection and transmission result from solving these boundary conditions in the absence of any sources.

A typical metasurface is an array of nanoparticles patterned on top of such a boundary between dielectric media (typically air and glass). One can then model the nanoparticles as an infinitesimally thin film of polarizable islands [50]. The presence of this film modifies the field boundary conditions, and solving those allows one to obtain new Fresnel coefficients that include contributions from the nanoparticle inclusions.

This model, when including only electric polarization, has been used extensively to model the optical response of thin layers [51–54].

We divide space into two regions with permittivities and permeabilities ε_1, μ_1 and ε_2, μ_2, respectively. The boundary conditions for the components tangential to the interface are, when disregarding any out-of-plane polarization and magnetization [24, 51]

$$\hat{\boldsymbol{z}} \times \left(\boldsymbol{E}_2 - \boldsymbol{E}_1\right) = \mu_0 \frac{\partial \boldsymbol{M}_\parallel^{\mathrm{s}}}{\partial t} \,, \tag{4.15}$$

$$\hat{\boldsymbol{z}} \times \left(\boldsymbol{H}_2 - \boldsymbol{H}_1\right) = -\frac{\partial \boldsymbol{P}_\parallel^{\mathrm{s}}}{\partial t} \,. \tag{4.16}$$

Here, we have chosen $\hat{\boldsymbol{z}}$ as a normal vector to the interface directed into medium 1, $\boldsymbol{M}_\parallel^{\mathrm{s}}$ and $\boldsymbol{P}_\parallel^{\mathrm{s}}$ are surface magnetizations and surface polarizations.

The choice to neglect the z-components is definitely justified in the case of metasurfaces with very thin particles, such as plasmonic nanodisks studied in previous works [53, 55]. For the case of the thicker silicon nanopillars studied in paper III, this approximation is less justified. However, experiments are well described by this model despite the omission of the z-components. A complete model taking all components into account is in the process of being developed.

We choose to use the surface excess quantities in eqns. (4.15) and (4.16) to model the nanoparticles present at the interface. Each nanoparticle has polarizabilities defined such that its electric and magnetic dipole moments

are

$$\boldsymbol{p} = \vec{\boldsymbol{\alpha}}^{\,\text{e}} \cdot \boldsymbol{E}^{\text{exc}} , \tag{4.17}$$

$$\boldsymbol{m} = \vec{\boldsymbol{\alpha}}^{\,\text{m}} \cdot \boldsymbol{H}^{\text{exc}} . \tag{4.18}$$

where $\boldsymbol{E}^{\text{exc}}$ and $\boldsymbol{H}^{\text{exc}}$ are the exciting electric and magnetic fields at the site of the particle, respectively. Denoting the particle density on the surface by ρ, the surface polarization (dipole moment per unit area) and surface magnetization are

$$\boldsymbol{P}^{\text{s}}_{\parallel} = \rho \alpha^{\text{e}}_{\parallel} \boldsymbol{E}^{\text{exc}}_{\parallel} , \tag{4.19}$$

$$\boldsymbol{M}^{\text{s}}_{\parallel} = \rho \alpha^{\text{m}}_{\parallel} \boldsymbol{H}^{\text{exc}}_{\parallel} , \tag{4.20}$$

where we assumed that the nanoparticles are isotropic in-plane so that the polarizability tensor becomes scalar. The boundary conditions in eqns. (4.15) and (4.16) become

$$\hat{\boldsymbol{z}} \times \left(\boldsymbol{E}_2 - \boldsymbol{E}_1 \right) = -\mathrm{i}\omega\mu_0 \rho \alpha^{\text{m}}_{\parallel} \boldsymbol{H}^{\text{exc}}_{\parallel} , \tag{4.21}$$

$$\hat{\boldsymbol{z}} \times \left(\boldsymbol{H}_2 - \boldsymbol{H}_1 \right) = \mathrm{i}\omega \rho \alpha^{\text{e}}_{\parallel} \boldsymbol{E}^{\text{exc}}_{\parallel} , \tag{4.22}$$

where we have assumed a harmonic time-dependence such that $\partial/\partial t \rightarrow -\mathrm{i}\omega\times$.

We now consider a situation plane-wave impinging on the interface from medium 1 so that

$$\boldsymbol{E}_{\text{inc}} = \boldsymbol{E}^i \mathrm{e}^{\mathrm{i}\boldsymbol{q}_{\parallel}\cdot\boldsymbol{r}_{\parallel} - \mathrm{i}p_1 z - \mathrm{i}\omega t} \tag{4.23}$$

$$\boldsymbol{H}_{\text{inc}} = \boldsymbol{H}^i \mathrm{e}^{\mathrm{i}\boldsymbol{q}_{\parallel}\cdot\boldsymbol{r}_{\parallel} - \mathrm{i}p_1 z - \mathrm{i}\omega t} = 1/Z_1 \hat{\boldsymbol{q}}^-_1 \times \boldsymbol{E}_{\text{inc}} \tag{4.24}$$

with analogous expressions for the reflected and transmitted fields. Here, $Z_1 = \sqrt{\mu_0\mu_1/\varepsilon_0\varepsilon_1}$ is the impedance in medium 1. The unit vectors $\boldsymbol{q}^{\pm}_j$, $\hat{\boldsymbol{s}}^{\pm}_j$ and $\hat{\boldsymbol{p}}^{\pm}_j$ for wave propagation in the direction of $\pm z$, as well as s- and p-polarization, are defined in the same way as in Sec. 4.1, Eqns. (4.4), (4.5) and (4.6). In both media, we have $q^2_{\parallel} + p^2_j = k^2_j = \varepsilon_j\mu_j\omega^2/c^2_0$.

Precisely at the interface, $z = 0$, all field are in phase and we have $\boldsymbol{E}_1 = \boldsymbol{E}_{\text{inc}} + \boldsymbol{E}_{\text{ref}} = \boldsymbol{E}^i + \boldsymbol{E}^r$ and $\boldsymbol{E}_2 = \boldsymbol{E}_{\text{tr}} = \boldsymbol{E}^t$ and analogously for the $\boldsymbol{H}$-fields. Since the electric and magnetic fields are discontinuous across the infinitesimally thin interface, a reasonable choice for the parallel part of the exciting fields is the mean value of the fields in either medium. The boundary conditions in eqns. (4.21) and (4.22) become

$$\hat{\boldsymbol{z}} \times \left[\boldsymbol{E}^t - (\boldsymbol{E}^i + \boldsymbol{E}^r) \right] = \frac{-\mathrm{i}\omega\mu_0 \rho \alpha^{\text{m}}_{\parallel}}{2} \left(\boldsymbol{H}^i_{\parallel} + \boldsymbol{H}^r_{\parallel} + \boldsymbol{H}^t_{\parallel} \right) , \tag{4.25}$$

$$\hat{\boldsymbol{z}} \times \left[\boldsymbol{H}^t - (\boldsymbol{H}^i + \boldsymbol{H}^r) \right] = \frac{\mathrm{i}\omega \rho \alpha^{\text{e}}_{\parallel}}{2} \left(\boldsymbol{E}^i_{\parallel} + \boldsymbol{E}^r_{\parallel} + \boldsymbol{E}^t_{\parallel} \right) . \tag{4.26}$$

We can now proceed to solve these boundary conditions to obtain reflection and transmission coefficients for s-polarized (TE) and p-polarized (TM) incidence separately. For each case, the boundary conditions each yield one equation. We introduce coefficients $r^s = E^r/E^i$ and $t^s = E^t/E^i$ and

analogously for p-polarization. The boundary conditions in the case of s-polarized incidence yield

$$t^s - (1 + r^s) = \frac{i\rho\alpha_\parallel^m}{2}\left(\frac{p_1}{\mu_1}(1 - r^s) + \frac{p_2}{\mu_2}t^s\right) , \qquad (4.27)$$

and

$$\frac{p_2}{\mu_2}t^s + \frac{p_1}{\mu_1}\left(-1 + r^s\right) = \frac{i\omega^2\mu_0\rho\alpha_\parallel^e}{2}\left(1 + r^s + t^s\right) . \qquad (4.28)$$

For the case of p-polarized incidence, they are

$$\frac{p_2}{k_2}t^p - \frac{p_1}{k_1}(1 - r^p) = \frac{i\rho\alpha_\parallel^m}{2}\left(\frac{k_1}{\mu_1}(1 + r^p) + \frac{k_2}{\mu_2}t^p\right) , \qquad (4.29)$$

and

$$\frac{k_2}{\mu_2}t^p - \frac{k_1}{\mu_1}(1 + r^p) = \frac{i\omega^2\mu_0\rho\alpha_\parallel^e}{2}\left(\frac{p_1}{k_1}(1 - r^p) + \frac{p_2}{k_2}t^p\right) . \qquad (4.30)$$

Solving these equations results the following expressions for the reflection and transmission coefficients

$$r^s = \frac{(p_1\mu_2 - p_2\mu_1)\left(1 - \frac{k_0^2\rho^2\alpha_\parallel^e\alpha_\parallel^m}{4\varepsilon_0}\right) - ip_1p_2\rho\alpha_\parallel^m + ik_0^2\mu_1\mu_2\rho\alpha_\parallel^e/\varepsilon_0}{(p_1\mu_2 + p_2\mu_1)\left(1 - \frac{k_0^2\rho^2\alpha_\parallel^e\alpha_\parallel^m}{4\varepsilon_0}\right) - ip_1p_2\rho\alpha_\parallel^m - ik_0^2\mu_1\mu_2\rho\alpha_\parallel^e/\varepsilon_0} , \qquad (4.31)$$

$$t^s = \frac{2p_1\mu_2\left(1 + \frac{k_0^2\rho^2\alpha_\parallel^e\alpha_\parallel^m}{4\varepsilon_0}\right)}{(p_1\mu_2 + p_2\mu_1)\left(1 - \frac{k_0^2\rho^2\alpha_\parallel^e\alpha_\parallel^m}{4\varepsilon_0}\right) - ip_1p_2\rho\alpha_\parallel^m - ik_0^2\mu_1\mu_2\rho\alpha_\parallel^e/\varepsilon_0} , \qquad (4.32)$$

and

$$r^p =$$

$$\frac{(\varepsilon_2 p_1\mu_1 - \varepsilon_1 p_2\mu_2)\left(1 - \frac{k_0^2\rho^2\alpha_\parallel^e\alpha_\parallel^m}{4\varepsilon_0}\right) + ik_0^2\varepsilon_1\varepsilon_2\rho\alpha_\parallel^m - i\mu_1\mu_2 p_1 p_2\rho\alpha_\parallel^e/\varepsilon_0}{(\varepsilon_2 p_1\mu_1 + \varepsilon_1 p_2\mu_2)\left(1 - \frac{k_0^2\rho^2\alpha_\parallel^e\alpha_\parallel^m}{4\varepsilon_0}\right) - ik_0^2\varepsilon_1\varepsilon_2\rho\alpha_\parallel^m - i\mu_1\mu_2 p_1 p_2\rho\alpha_\parallel^e/\varepsilon_0} , \qquad (4.33)$$

$$t^p =$$

$$\frac{2\sqrt{\varepsilon_1\varepsilon_2}\,p_1\mu_2\left(1 + \frac{k_0^2\rho^2\alpha_\parallel^e\alpha_\parallel^m}{4\varepsilon_0}\right)}{(\varepsilon_2 p_1\mu_1 + \varepsilon_1 p_2\mu_2)\left(1 - \frac{k_0^2\rho^2\alpha_\parallel^e\alpha_\parallel^m}{4\varepsilon_0}\right) - ik_0^2\varepsilon_1\varepsilon_2\rho\alpha_\parallel^m - i\mu_1\mu_2 p_1 p_2\rho\alpha_\parallel^e/\varepsilon_0} . \qquad (4.34)$$

The translation into angles of incidence and refraction is done through $p_1 = k_1\cos\theta_i$ and $p_2 = k_2\cos\theta_t$ where θ_i and θ_t are measured from substrate normal in their respective media.

From these equations, one can see that the total reflection transmission from the metasurface is a superposition of contributions from the interface

itself (the first terms in either numerator or denominator correspond to the standard Fresnel coefficients) and contributions from the scattering of the electric dipoles and the magnetic dipoles.

4.3 Coupled-Dipole Approximation (CDA)

In the previous chapters, we have focused on the properties of a single nanoparticle. When many such particles are brought together, for example on top of a metasurface or in a colloidal solution, interaction between the particles can become important. In the previous section, we described a method to characterize a metasurface using surface averaged polarizations and magnetizations. While it is possible to define effective polarizabilities for the particles that take the average interparticle interaction into account, one cannot in this model capture any effects that depend on the precise location of the nanoparticles.

In general, each particle in an ensemble is located in the superposition of the incident field and the scattered field from each other particle. This interaction between particles is responsible for the extreme field enhancements that arise in the gap between two closely placed nanostructures. Many applications make use of this strong field enhancement. Examples include surface-enhanced Raman spectroscopy [12, 22, 56] and enhanced fluorescence [57].

Some of this interaction can be taken into account through the so-called coupled dipole approximation (CDA) [26, 58, 59]. In this picture, each nanoparticle is regarded as a point dipole in the presence of the incident field and the retarded dipole field from all other nanoparticles. The dipole moment for dipole i becomes

$$\boldsymbol{p}_i = \overleftrightarrow{\boldsymbol{\alpha}}_i \cdot \left(\boldsymbol{E}_{\mathrm{inc},i} + \omega^2 \mu_0 \mu_m \sum_{j \neq i} \overleftrightarrow{\boldsymbol{G}}(\boldsymbol{r}_i, \boldsymbol{r}_j) \cdot \boldsymbol{p}_j \right), \qquad (4.35)$$

where $\overleftrightarrow{\boldsymbol{\alpha}}_i$ is the polarizability tensor (with any depolarization taken into account) of the ith dipole, $\boldsymbol{E}_{\mathrm{inc},i}$ is the incident field at the location of dipole i and $\omega^2 \mu_0 \mu_m \overleftrightarrow{\boldsymbol{G}}(\boldsymbol{r}_i, \boldsymbol{r}_j) \cdot \boldsymbol{p}_j$ is the scattered field *from* dipole j at the location of dipole i, with $\overleftrightarrow{\boldsymbol{G}}(\boldsymbol{r}_i, \boldsymbol{r}_j)$ being the Greens' function tensor of the medium. If we define a tensor, $\overleftrightarrow{\boldsymbol{A}}$, such that

$$\overleftrightarrow{\boldsymbol{A}}_{ij} = \begin{cases} \overleftrightarrow{\boldsymbol{\alpha}}_i^{-1} & \text{for } j = i\,, \\ -\omega^2 \mu_0 \mu_m \overleftrightarrow{\boldsymbol{G}}(\boldsymbol{r}_i, \boldsymbol{r}_j) & \text{for } j \neq i\,, \end{cases} \qquad (4.36)$$

the equation for the dipole moments can be written as a linear system of equations according to

$$\sum_{j=1}^{N} \overleftrightarrow{\boldsymbol{A}}_{ij} \cdot \boldsymbol{p}_j = \boldsymbol{E}_{\mathrm{inc},i}\,. \qquad (4.37)$$

For a homogeneous medium, we have [25, 46]

$$\vec{\vec{G}}_h(\boldsymbol{r}_i, \boldsymbol{r}_j) =$$
$$\left(\frac{k_m^2 R^2 + \mathrm{i}k_m R - 1}{k_m^2 R^2} \mathbb{1} + \frac{3 - 3\mathrm{i}k_m R - k_m^2 R^2}{k_m^2 R^2} \hat{\boldsymbol{R}} \otimes \hat{\boldsymbol{R}} \right) \frac{\mathrm{e}^{\mathrm{i}k_m R}}{4\pi R} , \quad (4.38)$$

where $\boldsymbol{R} = \boldsymbol{r}_j - \boldsymbol{r}_i$ and $\otimes$ denotes the dyadic (or outer) product. For column vectors, $\boldsymbol{v} \otimes \boldsymbol{v} = \boldsymbol{v}\boldsymbol{v}^T$.

The approximation of treating each nanoparticle as a point dipole is a valid one for small enough particles that are not too closely spaced [60]. In these cases, higher multipole orders come into play.

The CDA model provides an approximation of the optical dipolar response of an array of nanoparticles. The strength of the model resides in the fact that it reduces the scattering problem to the solution of a system of linear equations. This problem is so ubiquitous that many efficient algorithms have been developed to tackle it. With the constant advances in computing power, larger and larger systems can be solved efficiently.

4.4 Finite Difference Time-Domain method (FDTD)

The finite difference time-domain method introduced by Yee in 1968 [61] is a powerful technique which allows for the approximate solution of electromagnetic problems. The method is based on solving the time-dependent Maxwell equations in the wake of an electromagnetic pulse in the time-domain. The solution is iterated in time until a steady state is reached in the electromagnetic fields. In the work presented in this thesis, the commercially available software FDTD Solutions (Lumerical Inc., Canada) has been used for calculations of optical properties of plasmonic as well as dielectric structures.

In the software, the time-dependent Maxwell equations are solved in a simulation region in which the scatterers are defined as geometrical objects with a certain dielectric function. At the edge of the simulation region, a set of boundary conditions are employed, typically either periodic or absorbing. The absorbing boundary conditions are meant to simulate a situation where the outgoing fields propagate to infinity and stop interacting with the scatterers.

A few things are worth noting about FDTD that stand in contrast to other methods typically used (e.g. the Finite Element Method (FEM)):

- Since FDTD is a time-domain method, injection of a broadband pulse makes the optical response for a spectrum of frequencies available from a single simulation through Fourier transforms. The broadband response of nanoparticles and metasurfaces is often of interest, making this a very useful property.

- The dielectric functions cannot be directly imported from tabulated, experimental values in the frequency domain. These need to be fitted using a combination of functions (for example Drude or Lorentzian functions). The dielectric functions need to fulfil the Kramers-Kronig relations (causality) [25]. However, a combination of these functions can most often be fitted to experimental data in the spectral region

of interest. Most commercial software implementations handle this
fitting internally.

- It is not straightforward to simulate oblique plane wave incidence
  when the translational symmetry in the z-direction is broken by a sub-
  strate. This is because the plane wave source injects fields that have a
  constant in plane wave-vector $\boldsymbol{k}_{\parallel}$ at all frequencies. This results in a
  frequency dependent incidence angle. This can be solved by perform-
  ing several simulations for different angles of incidence.

4.5   Optical measurements

Metasurfaces are generally composed of nanoparticles smaller than the in-
cident light wavelength. In addition, they are patterned such that the inter-
particle distances are subwavelength. The scattered field from all nanopar-
ticles is only exactly in phase in the forward direction and specular reflec-
tion direction ($\boldsymbol{k}_{\parallel}^{\mathrm{scat}} = \boldsymbol{k}_{\parallel}^{\mathrm{inc}}$). As a result, rather than scattering like a collec-
tion of individual dipole scatterers, the far-field from such an arrangement
is concentrated in these directions. Diffuse scattering from typical meta-
surfaces fabricated by colloidal lithography is strongly suppressed, albeit
measurable, as shown in paper III and Ref. [32]. Most of the scattering in-
formation about the metasurfaces can thus be obtained by measuring trans-
mission and reflection.

Measuring the light transmitted through a metasurface yields the ex-
tinction. The light which is not transmitted is either absorbed or scattered
(mostly reflected). The extinction is thus given by

$$E = 1 - T \,, \tag{4.39}$$

where T is the transmittance through the sample. For this to correspond to
the extinction from the particles alone, one needs to reference the transmis-
sion against a bare glass slide to account for the reflection from the interface
as well as the spectrum of the lamp and any properties of the optical com-
ponents.

The extinction is typically measured at normal incidence, see Fig. 4.3(a),
although any angle dependence is easily probed by tilting the sample. In
this configuration, one can also measure the reflection at normal incidence
by adding a 50/50 beamsplitter.

Figure 4.3(b) shows the experimental set-up for measuring reflection
from a metasurface. The sample is mounted on a hemispherical prism us-
ing refractive index matching oil.

Both these measurement set-ups were used to characterize metasurfaces
of silicon nanopillars in appended paper III. In these experiments, reference
was taken using a silver mirror and thus the metasurface (glass interface +
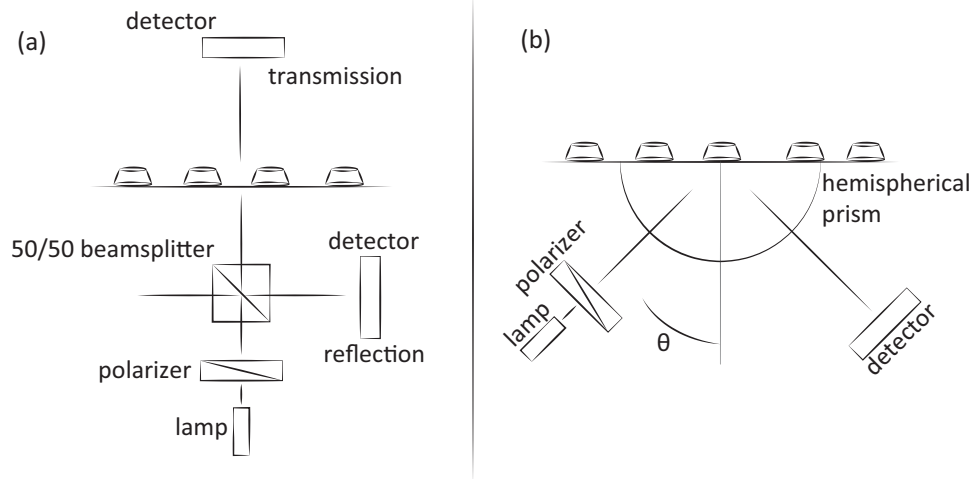nanoparticles) is considered as a single entity.

FIGURE 4.3: (a) Normal incidence reflection and transmission measurements. (b) Experimental set-up for measuring specular reflection.

Chapter 5

Summary and outlook

As we have seen in the work presented in this thesis, the interaction between light and nanostructured matter exhibit many interesting effects that are useful for many applications.

It has been the focus of this thesis to elucidate the properties of metasurfaces. Properties of metasurfaces composed of either plasmonic or high-index nanoparticles have been explored, both at the level of individual particles and their collective behaviour. Chapters 2 and 3 dealt with the properties of the single plasmonic and high-index nanoparticle scatterers, respectively. Assembling the particles into metasurfaces introduces collective properties, both in terms of far-field coherent scattering and near-field coupling. The thin homogeneous film approach presented through the island-film theory in Sec. 4.2 addresses the collective scattering by introducing modified coefficients for reflection and transmission of plane waves. However, any inter-particle coupling that depends on the exact location of the scatterers is not captured by this model.

By employing the Coupled Dipole Approximation (Sec. 4.3) to find the optical response of a small part of a metasurface and propagate the resulting dipole scattering into the far-field, one can take some of the particle-particle interaction into account. One potential future direction is to compare these results to the island-film theory to give an indication of the validity of the thin-film approximation in different particle density regimes.

In the implementation of the island-film theory discussed in Chapter 3, a few approximations and simplifications were made. Firstly, the out-of-plane components of the polarizability of the nanoparticles were neglected. This approximation is valid for thin particles, where the out-of-plane components are weak and shifted to higher energies. For thicker particles, however, the contribution from the z-component can become important. Secondly, the particles studied were symmetric in-plane, so the polarizabilities were scalar. An extension of the model to include the out-of-plane polarizations and magnetizations as well as the potential for anisotropic particles would reduce the tractability of the expressions, but would be useful for continued modelling.

The low cost, high throughput fabrication method used to produce the silicon nanopillars studied in paper III can easily be extended to metasurfaces composed of structures with different geometries. Realized examples include chiral crescents and dimer structures (see Figure 5.1). This adaptation enables the continued study of various silicon metasurfaces and we plan to study these geometries in detail and use them for different applications and light management.
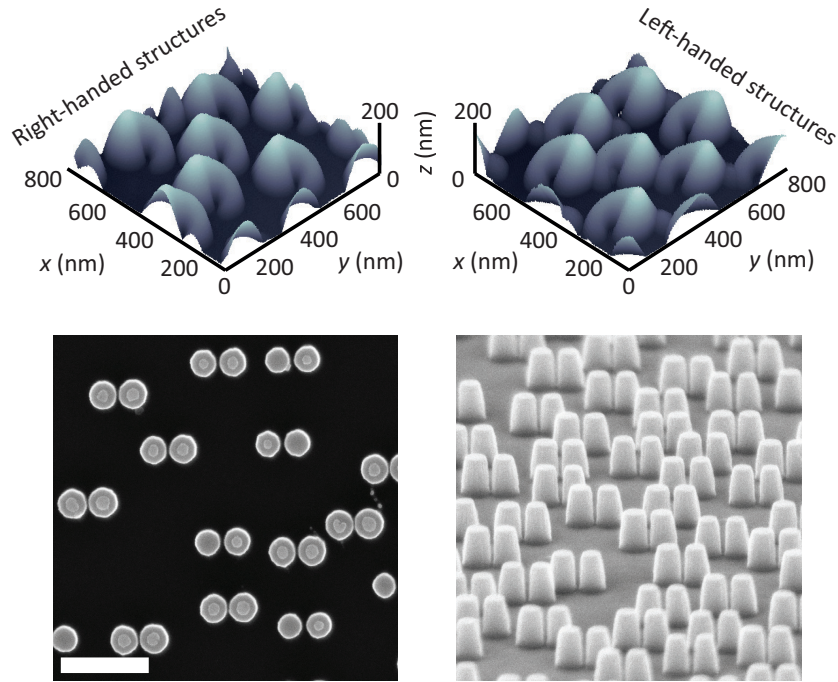
FIGURE 5.1: AFM and SEM images of different structures fabricated with colloidal lithography from polycrystalline silicon wafers on glass. (Top) AFM images of chiral crescent nanostructures. (Bottom) SEM images of silicon nanodimers. The scale bar corresponds to 500 nm.

In addition, combining the potentially high-quality factor resonances found in high-index nanoparticles with the strong field enhancements of plasmonic nanoparticles may open doors to new applications. With the help of methods such as FDTD, we plan explore these combined geometries in an effort to unveil novel effects such as directionality, increased sensor efficiency and exotic near-field coupling.

In conclusion, metasurface research is bustling with activity and realization of many new and interesting functionalities is within the reach of current nanofabrication techniques.

Bibliography

1. Englebienne, P. Use of colloidal gold surface plasmon resonance peak shift to infer affinity constants from the interactions between protein antigens and antibodies specific for single or multiple epitopes. *Analyst* **123,** 1599–1603. ISSN: 0003-2654 (1998).

2. Liu, N., Tang, M. L., Hentschel, M., Giessen, H. & Alivisatos, A. P. Nanoantenna-enhanced gas sensing in a single tailored nanofocus. *Nat Mater* **10,** 631–636. ISSN: 1476-1122 (2011).

3. Catchpole, K. R. & Polman, A. Plasmonic solar cells. *Optics Express* **16,** 21793–21800 (2008).

4. Yu, N. *et al.* Light Propagation with Phase Discontinuities: Generalized Laws of Reflection and Refraction. *Science* **334,** 333–337 (2011).

5. Ni, X., Emani, N. K., Kildishev, A. V., Boltasseva, A. & Shalaev, V. M. Broadband Light Bending with Plasmonic Nanoantennas. *Science* **335,** 427–427 (2012).

6. Aieta, F. *et al.* Aberration-Free Ultrathin Flat Lenses and Axicons at Telecom Wavelengths Based on Plasmonic Metasurfaces. *Nano Letters* **12,** 4932–4936. ISSN: 1530-6984 (2012).

7. Yu, N. *et al.* A Broadband, Background-Free Quarter-Wave Plate Based on Plasmonic Metasurfaces. *Nano Letters* **12,** 6328–6333. ISSN: 1530-6984 (2012).

8. Huang, L. *et al.* Three-dimensional optical holography using a plasmonic metasurface. *Nature Communications* **4,** 2808 (2013).

9. McFarland, A. D. & Van Duyne, R. P. Single Silver Nanoparticles as Real-Time Optical Sensors with Zeptomole Sensitivity. *Nano Letters* **3,** 1057–1062. ISSN: 1530-6984 (2003).

10. Haes, A. J. *et al.* Plasmonic Materials for Surface-Enhanced Sensing and Spectroscopy. *MRS Bulletin* **30,** 368–375 (2005).

11. Svedendahl, M., Verre, R. & Käll, M. Refractometric biosensing based on optical phase flips in sparse and short-range-ordered nanoplasmonic layers. *Light Sci Appl* **3,** e220 (2014).

12. Xu, H., Bjerneld, E. J., Käll, M. & Börjesson, L. Spectroscopy of Single Hemoglobin Molecules by Surface Enhanced Raman Scattering. *Physical Review Letters* **83,** 4357–4360 (1999).

13. Paniagua-Domínguez, R. *et al.* Generalized Brewster effect in dielectric metasurfaces. *Nature Communications* **7,** 10362 (2016).

14. Yang, Y., Kravchenko, I. I., Briggs, D. P. & Valentine, J. All-dielectric metasurface analogue of electromagnetically induced transparency. *Nature Communications* **5,** 5753 (2014).

15. Caldarola, M. *et al.* Non-plasmonic nanoantennas for surface enhanced spectroscopies with ultra-low heat conversion. *Nature Communications* **6,** 7915 (2015).

16. Fan, W., Yan, B., Wang, Z. & Wu, L. Three-dimensional all-dielectric metamaterial solid immersion lens for subwavelength imaging at visible frequencies. *Science Advances* **2.** doi:`10.1126/sciadv.1600901` (2016).

17. Fredriksson, H. *et al.* Hole–Mask Colloidal Lithography. *Advanced Materials* **19,** 4297–4302. ISSN: 1521-4095 (2007).

18. Sommerfeld, A. Ueber die Fortpflanzung elektrodynamischer Wellen längs eines Drahtes. *Annalen der Physik* **303,** 233–290. ISSN: 1521-3889 (1899).

19. Mie, G. Beiträge zur Optik trüber Medien, speziell kolloidaler Metallösungen. *Annalen der physik* **330,** 377–445. ISSN: 1521-3889 (1908).

20. Fano, U. The theory of anomalous diffraction gratings and of quasi-stationary waves on metallic surfaces (Sommerfeld's waves). *JOSA* **31,** 213–222 (1941).

21. Anker, J. N. *et al.* Biosensing with plasmonic nanosensors. *Nat Mater* **7,** 442–453. ISSN: 1476-1122 (2008).

22. Kneipp, K. *et al.* Single Molecule Detection Using Surface-Enhanced Raman Scattering (SERS). *Physical Review Letters* **78,** 1667–1670 (1997).

23. Drude, P. Zur elektronentheorie der metalle. *Annalen der Physik* **306,** 566–613. ISSN: 1521-3889 (1900).

24. Bohren, C. F. & Huffman, D. R. *Absorption and scattering of light by small particles* ISBN: 0-471-05772-X (John Wiley & Sons, 1983).

25. Jackson, J. D. *Classical electrodynamics* ISBN: 047130932X (Wiley, 1999).

26. Draine, B. T. The discrete-dipole approximation and its application to interstellar graphite grains. *The Astrophysical Journal* **333,** 848–872. ISSN: 0004-637X (1988).

27. Meier, M. & Wokaun, A. Enhanced fields on large metal particles: dynamic depolarization. *Optics Letters* **8,** 581–583 (1983).

28. Zeman, E. J. & Schatz, G. C. in *Dynamics on Surfaces: Proceedings of the Seventeenth Jerusalem Symposium on Quantum Chemistry and Biochemistry Held in Jerusalem, Israel, 30 April - 3 May, 1984* (eds Pullman, B., Jortner, J., Nitzan, A. & Gerber, B.) 413–424 (Springer Netherlands, Dordrecht, 1984). ISBN: 978-94-009-5237-9.

29. Nylander, C., Liedberg, B. & Lind, T. Gas detection by means of surface plasmon resonance. *Sensors and Actuators* **3,** 79–88. ISSN: 0250-6874 (1982).

30. Liedberg, B., Nylander, C. & Lunström, I. Surface plasmon resonance for gas detection and biosensing. *Sensors and Actuators* **4,** 299–304. ISSN: 0250-6874 (1983).

31. Homola, J. Surface Plasmon Resonance Sensors for Detection of Chemical and Biological Species. *Chemical Reviews* **108,** 462–493. ISSN: 0009-2665 (2008).

32. Svedendahl, M., Chen, S., Dmitriev, A. & Käll, M. Refractometric Sensing Using Propagating versus Localized Surface Plasmons: A Direct Comparison. *Nano Letters* **9,** 4428–4433. ISSN: 1530-6984 (2009).

33. Croissant, J. & Zink, J. I. Nanovalve-Controlled Cargo Release Activated by Plasmonic Heating. *Journal of the American Chemical Society* **134,** 7628–7631. ISSN: 0002-7863 (2012).

34. Hirsch, L. R. *et al.* Nanoshell-mediated near-infrared thermal therapy of tumors under magnetic resonance guidance. *Proceedings of the National Academy of Sciences* **100,** 13549–13554 (2003).

35. Zhao, Q., Zhou, J., Zhang, F. & Lippens, D. Mie resonance-based dielectric metamaterials. *Materials Today* **12,** 60–69. ISSN: 1369-7021 (2009).

36. Evlyukhin, A. B., Reinhardt, C., Seidel, A., Luk'yanchuk, B. S. & Chichkov, B. N. Optical response features of Si-nanoparticle arrays. *Physical Review B* **82,** 045404 (2010).

37. García-Etxarri, A. *et al.* Strong magnetic response of submicron Silicon particles in the infrared. *Optics Express* **19,** 4815–4826 (2011).

38. Person, S. *et al.* Demonstration of Zero Optical Backscattering from Single Nanoparticles. *Nano Letters* **13,** 1806–1809. ISSN: 1530-6984 (2013).

39. Geffrin, J. M. *et al.* Magnetic and electric coherence in forward- and back-scattered electromagnetic waves by a single dielectric subwavelength sphere. *Nature Communications* **3,** 1171 (2012).

40. Li, J. *et al.* All-Dielectric Antenna Wavelength Router with Bidirectional Scattering of Visible Light. *Nano Letters* **16,** 4396–4403. ISSN: 1530-6984 (2016).

41. Doyle, W. T. Optical properties of a suspension of metal spheres. *Physical Review B* **39,** 9852–9858 (1989).

42. Palik, E. D. *Handbook of optical constants of solids* ISBN: 0125444230 (Academic press, 1998).

43. Bludau, W., Onton, A. & Heinke, W. Temperature dependence of the band gap of silicon. *Journal of Applied Physics* **45,** 1846–1848 (1974).

44. Miroshnichenko, A. E., Evlyukhin, A. B., Kivshar, Y. S. & Chichkov, B. N. Substrate-Induced Resonant Magnetoelectric Effects for Dielectric Nanoparticles. *ACS Photonics* **2,** 1423–1428 (2015).

45. Novotny, L. & Hecht, B. *Principles of Nano-Optics* ISBN: 0-521-83224-1 (Cambridge University Press, 2006).

46. Johansson, P. Electromagnetic Green's function for layered systems: Applications to nanohole interactions in thin metal films. *Physical Review B* **83,** 195408 (2011).

47. Hecht, E. *Optics* 4th Edition. ISBN: 1-292-02157-8 (Pearson Education Ltd., 2004).

48. Arfken, G. B. & Weber, H. J. *Mathematical Methods for Physicists* ISBN: 0-12-059876-0 (Elsevier Academic Press, 2005).

49. Axelrod, D. Cell-substrate contacts illuminated by total internal reflection fluorescence. *The Journal of Cell Biology* **89,** 141–145 (1981).

50. Bedeaux, D. & Vlieger, J. *Optical properties of surfaces* ISBN: 1860944507 (World Scientific, 2004).

51. Lazzari, R. & Simonsen, I. GranFilm: a software for calculating thin-layer dielectric properties and Fresnel coefficients. *Thin Solid Films* **419,** 124–136. ISSN: 0040-6090 (2002).

52. Mendoza-Galván, A. *et al.* Optical response of supported gold nanodisks. *Optics Express* **19,** 12093–12107 (2011).

53. Svedendahl, M., Johansson, P. & Käll, M. Complete Light Annihilation in an Ultrathin Layer of Gold Nanoparticles. *Nano Letters* **13,** 3053–3058. ISSN: 1530-6984 (2013).

54. Ogier, R., Fang, Y., Käll, M. & Svedendahl, M. Near-Complete Photon Spin Selectivity in a Metasurface of Anisotropic Plasmonic Antennas. *Physical Review X* **5,** 041019 (2015).

55. Svedendahl, M. & Käll, M. Fano Interference between Localized Plasmons and Interface Reflections. *ACS Nano* **6,** 7533–7539. ISSN: 1936-0851 (2012).

56. Stiles, P. L., Dieringer, J. A., Shah, N. C. & Van Duyne, R. P. Surface-Enhanced Raman Spectroscopy. *Annual Review of Analytical Chemistry* **1,** 601–626. ISSN: 1936-1327 (2008).

57. Bek, A. *et al.* Fluorescence Enhancement in Hot Spots of AFM-Designed Gold Nanoparticle Sandwiches. *Nano Letters* **8,** 485–490. ISSN: 1530-6984 (2008).

58. Draine, B. T. & Goodman, J. Beyond Clausius-Mossotti: Wave propagation on a polarizable point lattice and the discrete dipole approximation. *The Astrophysical Journal* **405,** 685–697. ISSN: 0004-637X (1993).

59. Draine, B. T. & Flatau, P. J. Discrete-Dipole Approximation For Scattering Calculations. *Journal of the Optical Society of America A* **11,** 1491–1499 (1994).

60. Gunnarsson, L. *et al.* Confined Plasmons in Nanofabricated Single Silver Particle Pairs: Experimental Observations of Strong Interparticle Interactions. *The Journal of Physical Chemistry B* **109,** 1079–1087. ISSN: 1520-6106 (2005).

61. Kane, Y. Numerical solution of initial boundary value problems involving maxwell's equations in isotropic media. *IEEE Transactions on Antennas and Propagation* **14,** 302–307. ISSN: 0018-926X (1966).